A Fractional Step Solution Method for the Unsteady Incompressible Navier–Stokes Equations in Generalized Coordinate Systems

Moshe Rosenfeld

MCAT Institute, San Jose, California

Dochan Kwak

NASA Ames Research Center, Moffett Field, California

AND

Marcel Vinokur

Sterling Software, Palo Alto, California

A fractional step method is developed for solving the time-dependent three-dimensional incompressible Navier–Stokes equations in generalized coordinate systems. The primitive variable formulation uses the pressure, defined at the center of the computational cell, and the volume fluxes across the faces of the cells as the dependent variables, instead of the Cartesian components of the velocity. This choice is equivalent to using the contravariant velocity components in a staggered grid multiplied by the volume of the computational cell. The governing equations are discretized by finite volumes using a staggered mesh system. The solution of the continuity equation is decoupled from the momentum equations by a fractional step method which enforces mass conservation by solving a Poisson equation. This procedure, combined with a consistent approximation of the geometric quantities, is done to satisfy the discretized mass conservation equation to machine accuracy, as well as to gain the favorable convergence properties of the Poisson solver. The momentum equations are solved by an approximate factorization method, and a novel ZEBRA scheme with four-color ordering is devised for the efficient solution of the Poisson equation. Several two- and three-dimensional laminar test cases are computed and compared with other numerical and experimental results to validate the solution method. Good agreement is obtained in all cases.   © 1991 Academic Press, Inc.

1. Introduction

In simulating viscous incompressible flows, much effort has been directed to obtaining steady state solutions [1–3], partly because of limited computer resources. However, numerous interesting and important fluid flow phenomena are essentially time dependent, i.e., flow separation, vortex shedding, turbulence, turbo-

machinery flow, and flow in biological systems. Numerous time-dependent solutions of viscous incompressible flows have been reported for two-dimensional cases [4–6]. However, to obtain time-dependent solutions of realistic three-dimensional problems within a reasonable time, it is essential to have a computationally efficient flow solver. The need for such a general solver has been recognized, but only recently, with the advent of new-generation supercomputers, has it become an achievable goal. To date, only a limited number of unsteady, three-dimensional solutions of the incompressible Navier–Stokes equations in generalized coordinate systems have been reported [7]. Therefore, the purpose of the present study is to develop and validate an accurate, unsteady, viscous, incompressible flow solver for arbitrary geometries.

Direct solution of the discrete equations resulting from the incompressible Navier–Stokes equations is still impractical for general three-dimensional cases. An iterative solution is difficult because of the lack of a pressure time-derivative term in the continuity equation. Several approaches have been suggested to overcome this problem. In the pseudocompressibility method [1, 6–8] a fictitious time derivative of the pressure is added to the continuity equation so that the modified set of equations can be solved implicitly by marching in time. When a steady solution is reached, the original equations are recovered. Time accuracy can be achieved by using a dual time-stepping [8] or a pseudo time iterative procedure [6, 7], in which the solution at each time step is obtained by subiterations on a set of equations similar to what is devised for the steady pseudocompressibility method.

Another approach used in many incompressible flow computations is the fractional step (projection) method with its numerous variants [9–14]. The solution is advanced one time step in two (or more) stages. Usually, in the first stage the momentum equations are solved for an approximate velocity field which is not generally divergence-free. In the second stage, the pressure and the velocity fields are corrected to satisfy the continuity equation. This step leads to a Poisson equation with Neumann-type boundary conditions. An efficient solution of the Poisson equation is critical since it may consume a substantial portion of the total computing time. The present procedure is developed based on a fractional step approach. The variable definitions and the staggered mesh arrangement are chosen to facilitate the development of an efficient Poisson solver for curvilinear coordinates. A novel and efficient ZEBRA scheme with four-color ordering is devised for the nonorthogonal Poisson solver. Using this scheme, a multigrid acceleration procedure can be readily incorporated.

An important aspect of achieving accuracy in arbitrary domains is related to the method of discretization. For example, certain geometric identities have to be satisfied accurately in the discrete sense as well as in the continuous domain. In this respect, the finite-volume appoach can more easily yield accurate and conservative approximations than methods based on finite-differences [15]. Therefore, a finite-volume discretization method in a staggered grid has been used with a consistent approximation of the geometric quantities in generalized curvilinear coordinate systems.

Another important aspect related to the efficiency and the accuracy of the solution method is the choice of the dependent variables. The difficulties associated with the pressure may be eliminated by replacing the pressure with the vorticity vector. However, the order of the governing equations is increased with adverse effects on the computational time requirement, and the specification of the vorticity boundary conditions is not straightforward. The primitive variables are the natural dependent variables for general three-dimensional flow calculations. Most existing primitive-variable solution methods use the Cartesian velocity components to describe the velocity vector. Shyy *et al.* [3] used contravariant-type velocity components, but only in the second step of a fractional step method (the correction stage). In incompressible flow, most of the solution methods use a staggered mesh in order to prevent the problems associated with the "checkerboard" behavior of the pressure field [10]. The extension of this approach to generalized coordinate systems is not straightforward, since the Cartesian components of the velocity cannot be uniquely related to particular coordinate lines.

In the present study, the volume fluxes across each face of the computational cells are chosen as dependent variables, instead of the Cartesian components of the velocity. These variables correspond to the contravariant velocity components in a staggered grid multiplied by the volume of the computational cell, and they make possible a simple extension of the staggered grid approach to generalized curvilinear coordinate systems. Using this choice, the discretized mass conservation equation can be easily satisfied, with favorable effects on the convergence properties of the Poisson equation solver.

The governing equations in an integral form are given in Section 2. The finite-volume discretization procedure and the numerical solution method are elaborated in Sections 3 and 4, respectively. Computed results of several validation cases are compared with other numerical and experimental results in Section 5, followed by a summary in Section 6.

2. FORMULATION

The equations governing the flow of constant density isothermal incompressible fluids in a fixed control volume V with face S, are the conservation of mass

$$\oint_S d\mathbf{S} \cdot \mathbf{u} = 0, \tag{1}$$

and the conservation of momentum

$$\frac{d}{dt} \int_V \mathbf{u} \, dV = \oint_S d\mathbf{S} \cdot \bar{T}, \tag{2}$$

where $\mathbf{u}$ is the velocity vector, dV is a volume element, and $d\mathbf{S}$ is the area element vector. The tensor $\bar{T}$ is given by

$$\bar{T} = -\mathbf{u}\mathbf{u} - P\bar{I} + v[\nabla\mathbf{u} + (\nabla\mathbf{u})^\mathrm{T}], \tag{3}$$

for Newtonian fluids, where $\bar{I}$ is the identity tensor, $\nabla\mathbf{u}$ is the gradient of $\mathbf{u}$, and $(\cdot)^\mathrm{T}$ is the transpose operator. The pressure is P and v is the effective kinematic viscosity. The viscous terms are written in a form easily replaceable by a variable kinematic viscosity coefficient (turbulence models) or by certain non-Newtonian flow models.

By using the divergence theorem, Eqs. (1) and (2) can be written in an equivalent differential form. The integral formulation is perferred in the present work since a finite-volume discretization method is employed.

3. Discretization

Geometric Quantities

A general nonorthogonal coordinate system (ξ, η, ζ) is defined (discretely) by

$$\mathbf{r} = \mathbf{r}(\xi, \eta, \zeta), \tag{4}$$

where $\mathbf{r} = (x, y, z)^\mathrm{T}$ is the Cartesian coordinate system. In the present work, only fixed coordinate systems are considered, although the extension to moving coordinate systems is possible [16]. The *computational domain* (ξ, η, ζ) is divided into uniform primary cells with mesh size $\Delta\xi = \Delta\eta = \Delta\zeta = 1$, and the center of each primary cell corresponds to the indices i, j, k. In the finite-volume discretization procedure, the integral governing equations are approximated over the computational volumes in the *physical space*.

The face l of a cell is given by the vector quantity (Fig. 1)

$$\mathbf{S}^l = \frac{\partial \mathbf{r}}{\partial(l+1)} \times \frac{\partial \mathbf{r}}{\partial(l+2)}. \tag{5}$$

The computational coordinates $l = \xi, \eta,$ or ζ are in cyclic order and $\times$ is the cross product operator. The vector quantity $\mathbf{S}^l$ has the magnitude of the area of the face and a direction normal to it. The differential analog is $\mathbf{S}^l = (1/J)\,\nabla l$, where J is the Jacobian of the inverse of the transformation (4) and ∇l is the contravariant base vector.

As Vinokur [15] pointed out, an accurate discretization should satisfy certain geometric conservation laws. The condition that a cell is closed (a special case of (1)),
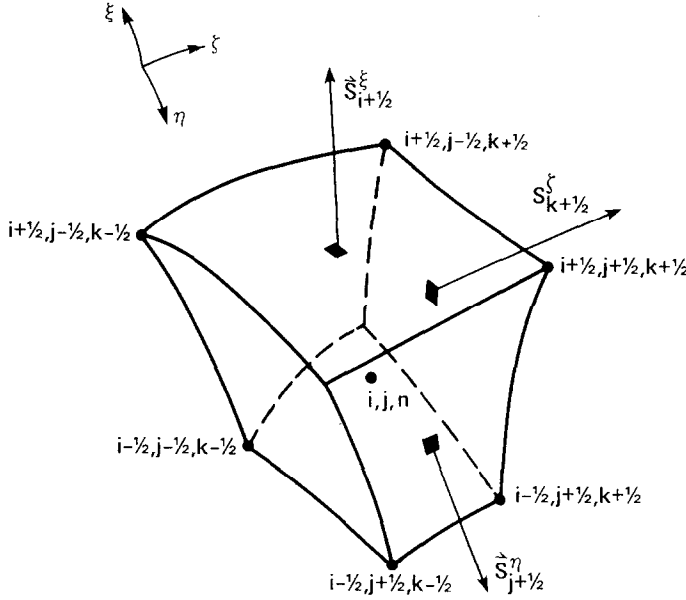
$$\oint_S d\mathbf{S} = 0 \tag{6a}$$

FIG. 1.   Definition of the primary cell.

should be satisfied exactly in the discrete form as well;

$$\sum_{\text{faces}} \mathbf{S}^l = 0, \tag{6b}$$

where the summation (with proper signs) is over all the faces of the computational cell. Equation (6b) may be satisfied by computing $\mathbf{S}^l$ from (5) at the center of each face by a proper approximation of $\partial \mathbf{r}/\partial l$. For example, the area vector $\mathbf{S}^\xi$, which is defined at to the point $(i + \frac{1}{2}, j, k)$, may be computed by using the second-order approximation

$$\left(\frac{\partial \mathbf{r}}{\partial \eta}\right)_{i+1/2} = \frac{1}{2}(\mathbf{r}_{j+1/2,\,k-1/2} - \mathbf{r}_{j-1/2,\,k-1/2} + \mathbf{r}_{j+1/2,\,k+1/2} - \mathbf{r}_{j-1/2,\,k+1/2})_{i+1/2},$$

$$\left(\frac{\partial \mathbf{r}}{\partial \zeta}\right)_{i+1/2} = \frac{1}{2}(\mathbf{r}_{j-1/2,\,k+1/2} - \mathbf{r}_{j-1/2,\,k-1/2} + \mathbf{r}_{j+1/2,\,k+1/2} - \mathbf{r}_{j+1/2,\,k-1/2})_{i+1/2}. \tag{7}$$

It is assumed that the coordinates of the cell vertices are given.

In order to ensure that the volumes of all the computational cells sum to the total volume, the volume of each cell is computed by dividing the cell into three pyramids having in common the main diagonal and one vertex of the cell [15]:

$$V = \frac{(\mathbf{S}^\xi_{i-1/2} + \mathbf{S}^\eta_{j-1/2} + \mathbf{S}^\zeta_{k-1/2})}{3} \cdot (\mathbf{r}_{i+1/2,\,j+1/2,\,k+1/2} - \mathbf{r}_{i-1/2,\,j-1/2,\,k-1/2}). \tag{8}$$

Note that the volume V of the cell is the inverse of the Jacobian: $V_{i,j,n} = 1/J_{i,j,n}$.

Mass Conservation

Discretization of the mass conservation equation (1) for a computational cell which coincides with the primary cell yields

$$(\mathbf{S}^\xi \cdot \mathbf{u})_{i+1/2} - (\mathbf{S}^\xi \cdot \mathbf{u})_{i-1/2} + (\mathbf{S}^\eta \cdot \mathbf{u})_{j+1/2} - (\mathbf{S}^\eta \cdot \mathbf{u})_{j-1/2}$$

$$+ (\mathbf{S}^\zeta \cdot \mathbf{u})_{k+1/2} - (\mathbf{S}^\zeta \cdot \mathbf{u})_{k-1/2} = \sum_{\text{faces}} \mathbf{S}^l \cdot \mathbf{u} = 0, \qquad (9)$$

where $\sum$ implies summation (with the proper signs) over all the faces of a computational cell. Note that throughout the present paper the indices (i, j, k) are omitted for simplicity whenever possible. Each term on the left-hand side of (9) approximates the volume flux over the corresponding face. Equation (9) states that the net mass flux (divided by the constant density) over each cell is zero, as no mass is generated within the cell. A discretized mass conservation equation, which is identical in form to the Cartesian case, can be derived if the volume fluxes over the faces of the computational cells are chosen as the unknowns instead of the Cartesian velocity components. Let

$$U^\xi = \mathbf{S}^\xi \cdot \mathbf{u},$$

$$U^\eta = \mathbf{S}^\eta \cdot \mathbf{u}, \qquad (10)$$

$$U^\zeta = \mathbf{S}^\zeta \cdot \mathbf{u},$$

where U^ξ, U^η, and U^ζ are the volume fluxes over the ξ, η, and ζ faces of a primary cell. Then, the continuity equation in any coordinate system takes the simple form

$$U^\xi_{i+1/2} - U^\xi_{i-1/2} + U^\eta_{j+1/2} - U^\eta_{j-1/2} + U^\zeta_{k+1/2} - U^\zeta_{k-1/2} = D_{iv}(U^l) = 0, \qquad (11)$$

where $U^l = (U^\xi, U^\eta, U^\zeta)$. The summation operator D_{iv} is a discrete divergence-like operator (the divergence operator itself is $(1/V) D_{iv}$). In tensor algebra nomenclature, U^l are the contravariant components of the velocity vector (in a staggered arrangement) multiplied by the volume V of the corresponding computational cell.

Accumulated experience with fractional step solution methods of unsteady flows shows the importance of exactly satisfying the discrete mass conservation equation, [10]. Therefore, the simple form of (11), which can be satisfied to round-off errors in any generalized coordinate system, suggests that the volume fluxes are the natural dependent variables in the context of fractional step methods. This choice complicates somewhat the discretization of the momentum equations, but is important for obtaining a divergence-free velocity field in generalized coordinate systems.

Summing (11) over all the cells yields the global mass conservation equation

$$\sum_B U^l = 0, \qquad (12)$$

where $\sum_B$ implies summation (with the proper signs) over all the boundaries of the

computational domain. If velocity components are specified as the boundary conditions over all the boundaries, consistency requires the exact satisfaction of the discrete equation (12).

Momentum Conservation

Spatial discretization of the integral momentum conservation equation (2) applied on a cell with constant volume V yields

$$V \frac{d\mathbf{u}}{dt} = \sum_l \mathbf{S}^l \cdot \bar{T} = \mathbf{F}. \tag{13}$$

The momentum equations should be reformulated so that the volume fluxes U^l will be the dependent variables. This can be done by a scalar multiplication of the vector momentum equations with the corresponding face area vector $\mathbf{S}^l$. Hence, the momentum equations are projected onto the direction of the corresponding face area vector $\mathbf{S}^l$ (and multiplied by its magnitude). This projection may have a favorable numerical effect provided the coordinate system is approximately aligned with the flow field. The discretization of the momentum equations for each U^l is performed on a different computational cell. Each cell has the formal size of $\Delta\xi \times \Delta\eta \times \Delta\zeta$ in the computational space, but the centers are located at $(i + \frac{1}{2}, j, k)$, $(i, j + \frac{1}{2}, k)$, and $(i, j, k + \frac{1}{2})$ for the U^ξ, U^η, and U^ζ momentum equations, respectively. This choice is in accordance with the conventional staggered-grid discretization practice.
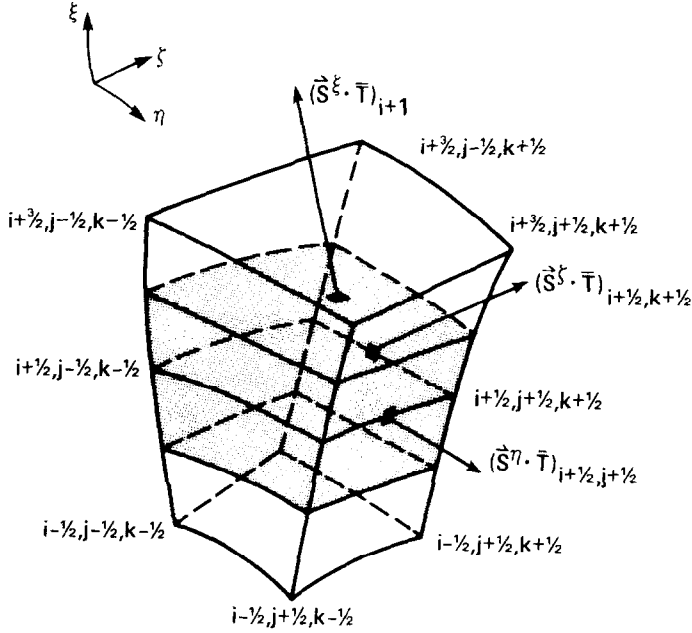
The derivation of the ξ-momentum equation will be described in this section. The other two momentum equations can be obtained by cyclic permutation.

The control volume used for the discretization of the U^ξ-momentum equation is shown as the shaded region in Fig. 2. The center of the cell is marked by the indices $(i + \frac{1}{2}, j, k)$. Dotting $\mathbf{S}^\xi_{i+1/2}$ with (13) yields

$$\mathbf{S}^\xi_{i+1/2} \cdot \left(V \frac{d\mathbf{u}}{dt} \right)_{i+1/2} = V_{i+1/2} \frac{dU^\xi_{i+1/2}}{dt} = \mathbf{S}^\xi_{i+1/2} \cdot \mathbf{F}_{i+1/2} \tag{14}$$

for a fixed grid. The term $\mathbf{F}_{i+1/2}$ is the total flux through the computational cell of the ξ-momentum equation. The evaluation of $\mathbf{F}_{i+1/2}$ requires three times more computational work than the standard scalar version since the flux *vector* should be computed on each face.

The static pressure P and the effective kinematic viscosity v are defined at the center (i, j, k) of each primary cell. The definition of the discrete pressure at this point is important for obtaining the standard second-order approximation of the Poisson equation, which is derived in the process of the fractional step solution of the discrete equations (see Section 4). The present definition of the volume fluxes and the midcell location of the pressure are equivalent to the staggered formulation of conventional fractional step solution methods.

FIG. 2. The computational cell (shaded) of the ξ-momentum equation.

In the following subsections, the temporal and the spatial discretization of the U^ξ-momentum equation will be elaborated separately.

Temporal Discretization

The U^ξ-momentum equation (14) is rewritten in operator form as

$$V_{i+1/2} \frac{dU^\xi_{i+1/2}}{dt} = L_\xi, \tag{15}$$

where L_ξ includes the right-hand-side terms of Eq. (14). For numerical reasons, the operator L_ξ must be split into several parts, which should be treated differently in the process of the time-discretization and the numerical solution

$$L_\xi = C_\xi(U^I) + R_\xi(P) + D_\xi(U^I) + D_{\xi,e}(U^I). \tag{16}$$

The convection terms are included in the nonlinear operator $C_\xi(U^I)$, and the operator $R_\xi(P)$ includes the pressure terms. The linear operators $D_\xi(U^I)$ and $D_{\xi,e}(U^I)$ are the implicit and explicit parts of the diffusion terms, respectively. The approximate factorization solution method (see Section 4) and the numerical solution of the momentum equations require explicit treatment of the diffusion terms, which do not fit a scalar tridiagonal pattern of the coefficient matrix of the approximate factorization steps.

A general second-order-accurate scheme, with explicit approximation of the convection and certain diffusion terms, is given by the three-time-level scheme

$$V_{i+1/2} \frac{(1+\varepsilon)(U^\xi)^{n+1} - (1+2\varepsilon)(U^\xi)^n + \varepsilon(U^\xi)^{n-1}}{\Delta t}$$

$$= \left(\frac{3}{2}+\varepsilon\right) L_\xi^n - \left(\frac{1}{2}+\varepsilon\right) L_\xi^{n-1}$$

$$+ \theta_r(R_\xi^{n+1} - 2R_\xi^n + R_\xi^{n-1}) + \theta_d(D_\xi^{n+1} - 2D_\xi^n + D_\xi^{n-1}), \qquad (17)$$

where n is the time level and ε, θ_r, and θ_d are parameters to be selected for a particular scheme. Higher-order approximations of the convection terms can be used without major additional computational cost because of its explicit approximation. The explicit approximation of the convection terms restricts the maximum allowable time step for stable solutions. This restriction may be too severe for steady solutions but acceptable for time-dependent solutions where physical reasons limit the time step anyway.

One of the simplest choices of the free parameters is $\theta_d = \theta_r = 0.5$, $\varepsilon = 0$ (Adams–Bashforth/Crank–Nicolson scheme). However, an analysis by Beam and Warming [17] demonstrates that the split form of a purely parabolic equation with explicit approximation of the mixed derivatives is not stable for this choice of parameters. Stable solutions may be achieved by a proper choice of ε, θ_r, and θ_d. Generally, the analysis of a simplified parabolic model problem shows that a necessary condition for the stability of the factored scheme is $\varepsilon > -\frac{1}{2}$, and $\theta \geqslant 2(1+\varepsilon)^2/(3+4\varepsilon)$ (for $\theta_d = \theta_r = \theta$) [17].

A more general scheme can be obtained by choosing $\Delta \mathscr{U}^\xi = (\Delta U^\xi)^n - \alpha_u(\Delta U^\xi)^{n-1}$ and $\Delta \mathscr{P} = \Delta P^n - \alpha_p \Delta P^{n-1}$ as the unknowns. Note that $\Delta \Phi^n = \Phi^{n+1} - \Phi^n$, where $\Phi = (U^\xi, P)$. Equation (17) takes the form

$$V_{i+1/2} \Delta \mathscr{U}^\xi = G + \frac{\Delta t}{1+\varepsilon} (\theta_d D_\xi(\Delta \mathscr{U}^I) + \theta_r R_\xi(\Delta \mathscr{P})), \qquad (18a)$$

where

$$G = \left(\frac{\varepsilon}{1+\varepsilon} - \alpha_u\right) V_{i+1/2}(\Delta U^\xi)^{n-1} + \frac{\Delta t}{1+\varepsilon}\left(\left(\frac{3}{2}+\varepsilon\right) L_\xi^n - \left(\frac{1}{2}+\varepsilon\right) L_\xi^{n-1}\right.$$

$$+ (\alpha_p - 1) \theta_r R_\xi(\Delta P)^{n-1} + (\alpha_u - 1) \theta_d D_\xi(\Delta U^\xi)^{n-1}\Big) \qquad (18b)$$

includes all the terms from the previous two time levels and the parameters α_u, α_p are to be selected. The choice $\alpha_u = \alpha_p = 0$ corresponds to the well known "delta form" where the unknowns are of order Δt, whereas $\alpha_u = \alpha_p = 1$ results in the most accurate scheme for an approximate factorization solution method since the unknowns are of order $(\Delta t)^2$.

Spatial Discretization

The finite-volume discretization of the ξ-momentum equation is performed on a cell centered at $(i + \frac{1}{2}, j, k)$, as is illustrated in Fig. 2. The time marching scheme (18) requires the computation of the operator L_ξ and of the linear operators R_ξ and D_ξ which also appear in the implicit part of (18a). For the time level n, L_ξ^n is defined by

$$L_\xi^n = \mathbf{S}_{i+1/2}^\xi \cdot \sum_l \mathbf{S}^l \cdot \bar{T}^n, \tag{19}$$

where the summation (with the proper signs) is over all the faces of the computational cell. To compute the fluxes over each face, the velocity vector should be computed from the volume-flux unknowns by the identity

$$\mathbf{u} = \mathbf{S}_\xi U^\xi + \mathbf{S}_\eta U^\eta + \mathbf{S}_\zeta U^\zeta = \mathbf{S}_m U^m. \tag{20}$$

From (10) and (20) one obtains

$$U^l = \mathbf{S}^l \cdot \mathbf{u} = \mathbf{S}^l \cdot \mathbf{S}_m U^m. \tag{21a}$$

The invariance of the velocity vector requires

$$\mathbf{S}^l \cdot \mathbf{S}_m = \delta_m^l, \tag{21b}$$

where δ_m^l is the Kronecker delta and $\mathbf{S}_m$ is the inverse base of $\mathbf{S}^l$. It has the differential analogue $\mathbf{S}_m = J(\partial \mathbf{r}/\partial m)$ so that in terms of tensor algebra, $\mathbf{S}_m$ is the covariant base vector multiplied by the Jacobian J, while $\mathbf{S}^l$ is the contravariant base vector multiplied by $1/J$. A uniform velocity field can be numerically preserved if the base $\mathbf{S}_m$ is computed at each point from the relation

$$\mathbf{S}_m = \frac{\mathbf{S}^{m+1} \times \mathbf{S}^{m+2}}{\mathbf{S}^m \cdot (\mathbf{S}^{m+1} \times \mathbf{S}^{m+2})} \tag{22}$$

which satisfies (21b) identically. Here m is the cyclic permutation of (ξ, η, ζ).

The ξ-face center of the U^ξ-momentum cell is at the point (i, j, k) (Fig. 2). The flux over this face is computed from

$$(\mathbf{S}^\xi \cdot \bar{T})_{i,j,k} = (-U^\xi U^l \mathbf{S}_l - \mathbf{S}^\xi P + \mathbf{S}^\xi \cdot \nu(\nabla \mathbf{u} + (\nabla \mathbf{u})^{\mathrm{T}}))_{i,j,k}. \tag{23}$$

The conservative form of the velocity vector gradient is

$$\nabla \mathbf{u} = \left(\oint_S d\mathbf{S}\mathbf{u} \right) \Big/ V. \tag{24}$$

Applying (24) to the computation of $\nabla \mathbf{u}_{i,j,k}$ yields

$$
\begin{aligned}
\nabla \mathbf{u}_{i,j,k} &= \frac{1}{V} (\mathbf{S}^{\xi}_{i+1/2} \mathbf{u}_{i+1/2} - \mathbf{S}^{\xi}_{i-1/2} \mathbf{u}_{i-1/2} \\
&\quad + \mathbf{S}^{\eta}_{j+1/2} \mathbf{u}_{j+1/2} - \mathbf{S}^{\eta}_{j\ 1/2} \mathbf{u}_{i-1/2} + \mathbf{S}^{\zeta}_{k+1/2} \mathbf{u}_{k+1/2} - \mathbf{S}^{\zeta}_{k\ 1/2} \mathbf{u}_{k-1/2}) \\
&= \frac{1}{V} (\mathbf{S}^{\xi}_{i+1/2} \mathbf{S}_{l,i+1/2} U^{l}_{i+1/2} - \mathbf{S}^{\xi}_{i-1/2} \mathbf{S}_{l,i-1/2} U^{l}_{i-1/2} \\
&\quad + \mathbf{S}^{\eta}_{j+1/2} \mathbf{S}_{l,j+1/2} U^{l}_{j+1/2} - \mathbf{S}^{\eta}_{j-1/2} \mathbf{S}_{l,j-1/2} U^{l}_{j-1/2} \\
&\quad + \mathbf{S}^{\zeta}_{k+1/2} \mathbf{S}_{l,k+1/2} U^{l}_{k+1/2} - \mathbf{S}^{\zeta}_{k-1/2} \mathbf{S}_{l,k-1/2} U^{l}_{k-1/2}).
\end{aligned} \tag{25}
$$

In the present work, the fluxes at the point (i, j, k) are computed by a second-order-accurate averaging and therefore the scheme is equivalent to second-order central differences. In some high Reynolds number cases, artificial diffusion should be added to smooth out the solution. In the present work, fourth-order numerical diffusion is implemented. In order to keep the conservation properties of the scheme, the artificial diffusion is formulated in terms of fluxes. Lower-order numerical diffusion is omitted in order to keep the second-order accuracy of the scheme and minimize the effect of the numerical diffusion.

The η- and ζ-face centers are at $(i+\frac{1}{2}, j-\frac{1}{2}, k)$ and $(i+\frac{1}{2}, j, k-\frac{1}{2})$, respectively. The fluxes over these faces are computed in a similar way (see details in [18]).

Geometrical Considerations

The approximation of the fluxes at the computational cell faces requires the determination of the geometric parameters $\mathbf{S}^{l}$ and $\mathbf{S}_{l}$ at numerous points for each computational cell. If uniform velocity is to be preserved, $\mathbf{S}_{l}$ should be evaluated at each point from (22) at the cost of more than 2000 additional operations for each cell. On the other hand, the available memory of present computers still imposes certain limitations on the number of geometric parameters that can be stored. In the present work, a compromise between CPU time and storage requirements has been made by storing only the quantities $\mathbf{S}^{\xi}_{i-1/2}$, $\mathbf{S}^{\eta}_{j-1/2}$, $\mathbf{S}^{\zeta}_{k-1/2}$, $\mathbf{S}_{\xi, i-1/2}$, $\mathbf{S}_{\eta, j-1/2}$, $\mathbf{S}_{\zeta, k\ 1/2}$, and $V_{i,j,k}$ for all the computational cells. The base $\mathbf{S}^{l}$ is computed from (5) while $\mathbf{S}_{l}$ is computed from (22).

The geometric quantities at other positions are computed by simple averaging. It can be shown [15] that this averaging satisfies the geometric conservation laws (closed cells and invariance of the total volume) even though a uniform free-stream velocity is not fully preserved since (22) is not satisfied at all points. In most cases the approximation of the $\mathbf{S}_{l}$ terms by simple averaging will not lead to a serious degradation of the results. This approximation affects only the computation of the momentum equation fluxes (the continuity equation is solved to machine accuracy). Near solid boundaries where large gradients usually occur, this approximation introduces only small errors, since a fine (and nearly orthogonal) mesh can be used. Far from a solid boundary, the velocity gradients are small (especially for external

flows) so the errors introduced by this approximation are small. Moreover, in these regions the flow is usually potential and therefore the continuity equation, which is not affected by this approximation at all, plays the major role. The accuracy of the approximation of the momentum equation is a less important factor in these regions. Further details on the various approximations are given in [18].

4. SOLUTION METHOD

The Fractional Step Method

The simultaneous solution of the large number of resulting discrete equations is very costly, especially for three-dimensional cases. An efficient approximate solution can be obtained by decoupling the solution of the momentum equations from the solution of the continuity equation by a fractional step method. The basic fractional step (or projection) method was proposed by Chorin [9]. The MAC method proposed earlier by Harlow and Welsh [14] is actually a variant of that method. The two methods are identical as long as the boundary conditions are not considered (see [19] for a detailed discussion of the relationship between the numerous variants of the fractional step method).

In the present implementation, first the momentum equations are solved for an approximate $\Delta \tilde{\mathcal{U}}^l$ by dropping $R_l(\Delta \mathcal{P})$ from (18), so that the pressure gradient is taken from the previous time-level

$$\left(V_{m+1/2} I - \frac{\theta_d \Delta t}{1+\varepsilon} D_l \right) \Delta \tilde{\mathcal{U}}^l = G, \tag{26a}$$

where I is the identity operator. The resulting flow field does not generally satisfy the mass conservation equation. In the second step $\Delta \mathcal{U}^l$ is updated by

$$V_{m+1/2}(\Delta \mathcal{U}^l - \Delta \tilde{\mathcal{U}}^l) = \frac{\theta_r \Delta t}{1+\varepsilon} R_l(\phi) \tag{26b}$$

so that the continuity equation (cast in terms of $\Delta \mathcal{U}^l$) will be satisfied at the level $n+1$,

$$D_{iv}[(U^l)^n + \alpha_u(\Delta U^l)^{n-1} + \Delta \mathcal{U}^l] = 0, \tag{26c}$$

where $m = i, j$ or n for $l = \xi, \eta,$ or ζ, respectively, and D_{iv} is the summation operator defined by (11). The variable ϕ is a scalar to be defined later.

Equations (26b) and (26c) are combined into a single discrete Poisson equation, which is easier to solve than the fully coupled set of the original equations, by applying the operator D_{iv} on (26b),

$$-\frac{1+\varepsilon}{\theta_r \Delta t} D_{iv}[(U^l)^n + \alpha_u(\Delta U^l)^{n-1} + \Delta \tilde{\mathcal{U}}^l] = D_{iv}\left(\frac{R_l(\phi)}{V_{m+1/2}}\right), \tag{26d}$$

since $D_{iv}((U^l)^{n+1}) = 0$. Note that the discrete Laplacian operator is given by $-(1/V) D_{iv}(R/V)$. Finally, the variables at the new time level $n+1$ are computed from

$$(U^l)^{n+1} = (U^l)^n + \alpha_u (\Delta U^l)^{n-1} + \Delta \mathcal{U}^l$$

$$\Delta \mathcal{P} = \phi \tag{26e}$$

$$P^{n+1} = P^n + \alpha_p \Delta P^{n-1} + \Delta \mathcal{P}.$$

Substituting $\Delta \tilde{\mathcal{U}}^l$ from (26b) into (26a) does not recover the original discrete momentum equation (18) if the substitution $\Delta \mathcal{P} = \phi$ is used, since the computation of the viscous terms in (26a) is based on $\Delta \tilde{\mathcal{U}}^l$ rather than on $\Delta \mathcal{U}^l$. It is shown in Appendix A that $(U^l)^{n+1}$ is the exact solution of the discrete equations, but $\Delta \mathcal{P} = \phi + O(\nu \Delta t)$ and therefore P^{k+1} is not the exact discrete solution. For a Cartesian case with $\varepsilon = 0$ and $\theta_d = \frac{1}{2}$, Kim and Moin [11] have derived the exact relation $\Delta \mathcal{P} = \phi - (\nu \Delta t/2) \nabla^2 \phi$, where ∇^2 is the Laplacian operator. However, such a simple relationship cannot be found in generalized coordinate systems with the present splitting of the diffusion terms (which does not satisfy certain vector identities). Braza *et al.* [20] have found (in the case of vortex shedding over a circular cylinder), insignificant differences between solutions which use the approximation $\Delta \mathcal{P} = \phi$, and solutions which compute the discrete pressure exactly although the approximate solution might be less stable. Because the difference between ϕ and $\Delta \mathcal{P}$ is proportional to ν, the direct substitution $\Delta \mathcal{P} = \phi$ is reasonable for high-Reynolds-number flows. This approximation degrades the second-order temporal accuracy of the pressure to first-order accuracy since this substitution is of the order $O(\Delta t)$. However, as can be seen from (26b), the velocity solution remains second-order accurate in time.

The first step (26a) is a consistent approximation of the momentum equations, i.e., as $(\Delta t, \Delta l) \to 0$, $(U^l)^{n+1} \to U^l$, where U^l is the solution of the continuous problem. Therefore, the physical boundary conditions may be specified from the $n+1$ time level. In some fractional step methods the substeps are not consistent and special boundary conditions should be devised for the intermediate steps [11].

The drawbacks of the present fractional step method are the increased storage required for the three-time-level method and the restriction on the maximal Courant number (CFL) due to the explicit treatment of the convection terms. The CFL number restriction is tolerable for many time-dependent solutions where the physics dictates a time step of the order CFL = 1, anyway. This restriction can be alleviated by including the convection terms in the implicit part.

The discrete momentum equations (26a) are solved by an approximate factorization method. The explicit treatment of some of the terms might degrade the stability of the method, especially for very skewed meshes. In the present method, special measures have been taken to alleviate these problems. The three-time-level discretization method improves the stability properties over the more commonly used

two-time-level methods, especially when mixed derivatives exist. The three-time-level scheme also maintains second-order accuracy in time, even for formulations which approximate certain terms explicitly [17].

Solution of the Poisson Equation

The discrete Poisson equation (26d) can be rewritten as

$$\mathscr{L}(\phi) = f, \tag{27a}$$

where the source term f is given by

$$f = -\frac{1+\varepsilon}{\theta_r \Delta t} D_{iv}((U^l)^n + \alpha_u(\Delta U^l)^{n-1} + \Delta \tilde{\mathscr{U}}^l). \tag{27b}$$

If Eqs. (26b) and (26c) are to be satisfied exactly, the Laplacian-like operator $\mathscr{L}$ should be computed *discretely* from the identity

$$\mathscr{L}(\phi) = D_{iv}\left(\frac{R_l(\phi)}{V_{m+1/2}}\right). \tag{27c}$$

The discrete divergence-like operator D_{iv} is defined in (11). The discrete gradient-like operator R_l is evaluated from the pressure terms which appear in the expressions for the computation of the fluxes. It is equal to the finite-volume approximation of the pressure gradient based on the scalar version of (24), dotted with S^l.

The normal-derivative (Neumann) type boundary conditions for each boundary l is computed from (26b),

$$R_l(\phi) = \frac{1+\varepsilon}{\theta_r \Delta t} V_{m+1/2}(\Delta \mathscr{U}^l - \Delta \tilde{\mathscr{U}}^l). \tag{27d}$$

At periodic boundaries, periodicity is used. If Dirichlet-type boundary conditions are specified for the velocities, condition (27d) is homogeneous. The compatibility condition necessary for the existence of a solution to a Poisson equation with derivative boundary conditions over all the boundaries, $\sum f = 0$, is automatically satisfied because of the imposed global *discrete* mass conservation (12). Note that "numerical" boundary conditions for the pressure are not required since the pressure is defined at the center of each cell.

An efficient solution of the Poisson equation is crucial for the efficiency of the whole solution method. For a general nonorthogonal coordinate system, the 19-point based discrete equations pose difficult challenges in obtaining fast solutions on vector computers. Many iterative methods cannot be efficiently vectorized and suffer from degradation of the convergence rate due to the sharp variation of the coefficients. The present solution method uses a novel application of a ZEBRA method with four-color ordering to decouple the implicit part of the algebraic equa-

tions and allow an effective vectorization of the Poisson solver, without deteriorating the convergence properties.

The three-dimensional ZEBRA scheme is an iterative solution scheme which solves implicitly all the equations along one coordinate line, say along ξ, as in the successive line over relaxation (SLOR) method. However, the order in which the lines are processed is not the usual lexicographic order (by rows or columns), but a "colored" order, devised so that the implicit solution of a line is decoupled from the solution of the other lines that belong to the same color. Most existing applications of the ZEBRA scheme use a two-color ordering ("red–black" schemes). This ordering is inappropriate for nonorthogonal cases. In the present method, the points in the (η, ζ) plane are classified into four groups and a different color label is given to each group (Fig. 3). First, all the "black" lines are swept in a lexicographic order, then the "red," "blue," and "green" lines, respectively. The implicit solution of a line is decoupled from the same color lines; for example, when solving for a "black" line, all the neighboring lines are of different color—"red," "blue," or "green." This arrangement enables an efficient vectorization of the method, even with the 19-point computational stencil. The implicit solution along the ξ coordinate line may be exploited to enhance convergence of problems with heavily clustered mesh points along that direction.
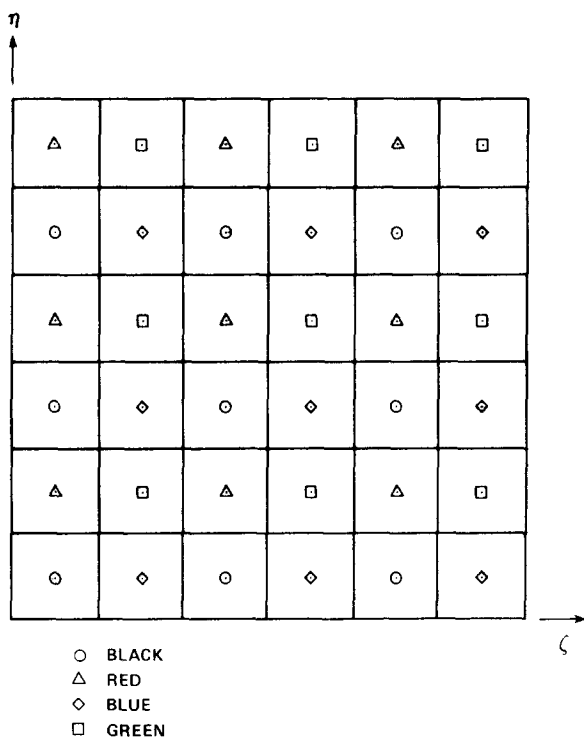
FIG. 3. The labeling of the points in the (η, ζ) plane for the Poisson equation solver.

A mathematical analysis of the ZEBRA method reveals that although each sweep of a color is equivalent to a line-Jacobi iteration, one complete iteration has the better convergence properties of the SLOR method. Therefore, the convergence properties of the present Poisson solver are similar to the SLOR method, but the required CPU time on a vector computer is significantly reduced because of the effective vectorization of the ZEBRA method. Moreover, the ZEBRA scheme has good smoothing properties and is nearly an optimal relaxation method for using a multigrid acceleration procedure.

A detailed study on the properties of the Poisson equation solver and a future implementation of a multigrid acceleration procedure will be reported in a separate paper.

5. RESULTS

Several representative cases have been solved to validate the solution procedure. The test cases include the flow in two- and three-dimensional driven cavities; the unsteady flow over a two-dimensional circular cylinder, with and without vortex shedding and the three-dimensional flow in a square duct with a $90°$ bend. Some steady cases are chosen as well, since most available experimental and numerical results are restricted to this regime. To fully validate unsteady solutions, it is necessary to establish data bases for time-dependent cases, in particular for three-dimensional configurations.

The basic ZEBRA solution method of the Poisson equation is implemented using an over-relaxation parameter determined expeirmentally. No difficulties were experienced in converging the Poisson equation to machine accuracy in any of the cases; consequently, a divergence-free velocity field could always be obtained. The convergence criterion for the maximal residual was set to 10^{-8}. That residual equals the divergence of the velocity multiplied by the volume of the computational cell (see (26d)), so the mass conservation equation divided by that volume is converged to the same order of magnitude.

A stability condition of the present solution method cannot be analytically derived. Numerical experiments shows that the method (without the addition of artificial diffusion) is stable for $CFL < f(Re)$, where CFL is the maximal Courant number defined by the maximum value of

$$CFL = \left(\frac{|u|}{\Delta x} + \frac{|v|}{\Delta y} + \frac{|w|}{\Delta z} \right) \Delta t = (|U^\xi| + |U^\eta| + |U^\zeta|) \frac{\Delta t}{V}, \tag{28}$$

over all the computational cells. The Cartesian velocity components are given by u, v, w, and $\Delta x, \Delta y, \Delta z$ are the physical mesh sizes in the corresponding directions and V is the volume of the computational cell. In the absence of fourth-order smoothing terms, the function $f(Re)$ is a monotonically decreasing function of the Reynolds number (*not* the cell Reynolds number). Usually, $f(Re) = 0.5 - 1$ results
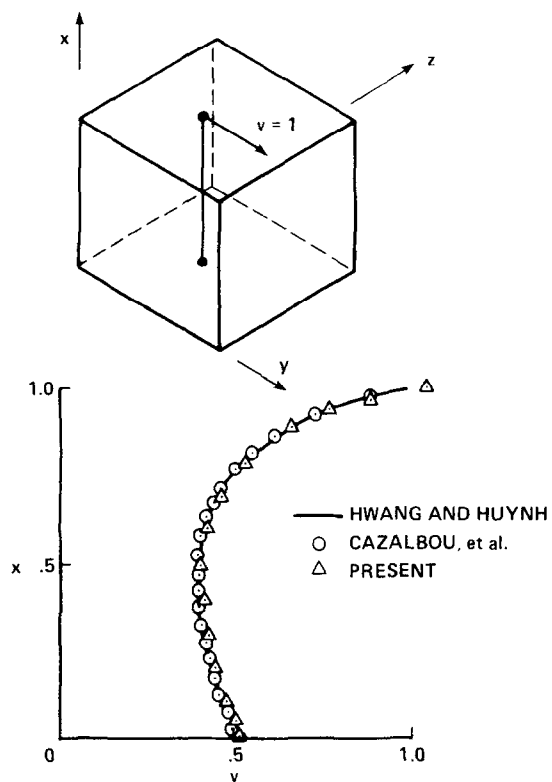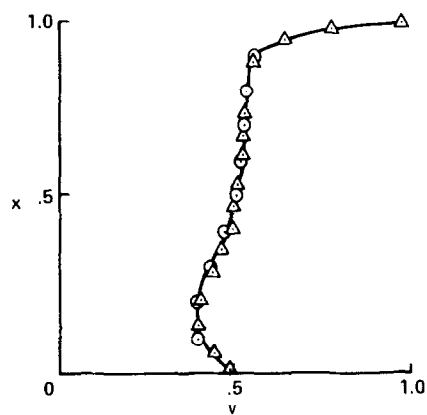
FIG. 4. Comparison of the horizontal velocity component along the vertical centerline of the cubic cavity.

in stable solutions. The maximum cell Reynolds number is of the order $10^1 - 10^2$ in all the computations. By adding fourth-order artificial diffusion terms, the time-step can be increased beyond this limit without introducing numerical instabilities.

The set of free parameters ε, θ_r, θ_d, α_u, and α_p can be adjusted to enhance the stability of the time-advancing scheme. In the present study no attempt was made to find the optimal values. In most of the test runs the following values were used: $\varepsilon = 0$, $\theta_r = 1$, $\theta_d = 1$, and $\alpha_u = \alpha_p = 0$.

Some convergence tests have been conducted to confirm the accuracy of the scheme by systematic refinement of the mesh size and the time-step. Both non-uniform Cartesian and generalized coordinate systems have been tested. The *discretized equations* are second-order accurate in both space and time. However, because of the substitution $\Delta \mathscr{P} = \phi$ (see Section 4), the temporal accuracy of the pressure is decreased to first order. The scheme was indeed found to be second-order accurate in space, and the second-order temporal accuracy of the velocity has been verified as well. The convergence tests show that the pressure is almost $\frac{3}{2}$-order accurate in time, which is better than the theoretical prediction.

The computer code is written for general three-dimensional problems. Two-dimensional cases are solved by using two intervals in the third direction and specifying periodic boundary conditions along that direction. The solution method consumes from 0.3 to $1 \cdot 10^{-3}$ CRAY-XMP CPU s/mesh-point/time-step, depending on the number of iterations required for the convergence of the Poisson solver. A substantial reduction in CPU time is anticipated by implementing a multigrid acceleration of the Poisson solver.
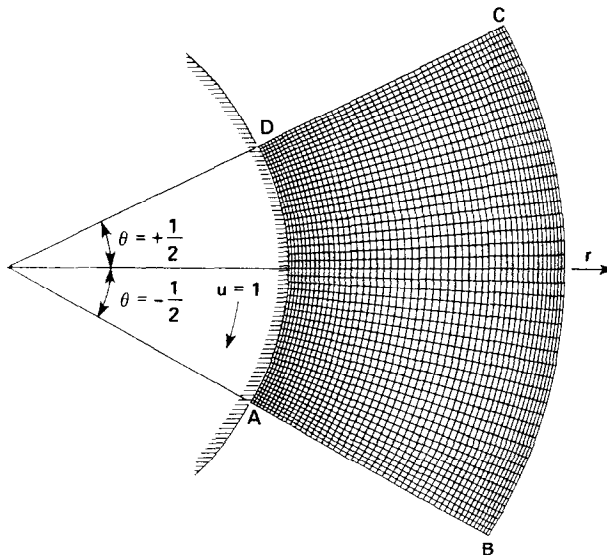

FIG. 5. The geometry and the mesh for the lid-driven polar cavity flow problem.

Selected results are presented in the following sections. Additional examples can be found in [18, 21].

Lid-Driven Cavity Flow

The flow field in a unit cubic lid-driven cavity was solved in several studies, i.e., [22, 23]. In the present work a uniformly distributed grid of $31 \times 31 \times 31$ points is used to advance the solution in time until a steady state is reached for $Re = 100$ and $Re = 1000$. The grid is identical with the one employed by Hwang and Huynh [23] so that a direct comparison can be made with their solution. The distribution of the y-component velocity along the geometric centerline ($y = z = 0.5$) is compared with
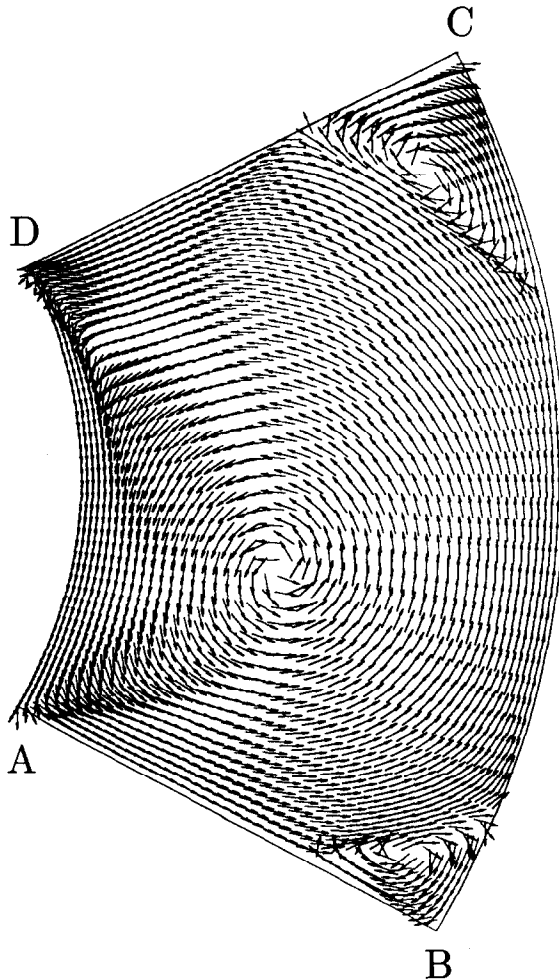
FIG. 6. Velocity direction for the polar cavity flow at $Re = 350$.

other numerical solutions [22, 23] in Fig. 4. Good agreement is obtained for both Reynolds numbers.

The two-dimensional lid-driven flow in a *polar cavity* was studied by Fuchs and Tillmark [24], both experimentally and numerically. This geometrically more challenging flow is also computed in the present study. Figure 5 shows the geometry of the problem and the $51 \times 51 \times 3$ mesh used in the present computation. The height AB of the cavity is equal to the radius of the boundary AD. A polar coordinate system is used with grid points clustered near the walls. Zero velocity is specified on all the boundaries, except on the AD boundary, where a unit tangential velocity is given.

The steady flow was computed for two Reynolds numbers, $Re = 60$ and $Re = 350$ (based on the height of the wall AB and the tangential velocity of the wall AD), for which experimental and numerical results are given in [24]. In the present paper, only the results for the higher Reynolds number will be described.

Figure 6 gives the velocity-direction plot (all velocity vectors are plotted with equal magnitude) for the $Re = 350$ case. The resulting flow field is similar to the two-dimensional square cavity flow. A main vortex and two secondary vortices are formed in the center and at the two corners B and C, respectively. The centers of the vortices agree with a flow visualization obtained by Fuchs and Tillmark [24] within an error of less than 2%. Figure 7 compares the radial and circumferential velocity components with the experimental results of Fuchs and Tillmark [24] along the three radial lines $\theta = -20°$, $0°$, and $20°$. Also shown are their numerical results obtained by a stream-function vorticity formulation written in a polar coordinate system. Generally, favorable agreement is obtained among all the results. Note in particular the very good agreement in the numerical results, although the present numerical results are obtained using about 2.5 times fewer mesh points. The grid points are more efficiently distributed in the present study than in the uniform grid employed by Fuchs and Tillmark [24]. The small deviation of the numerical results from the experimental results is probably because of the three-dimensional effects which were found in the experiment [24].

Flow over a Circular Cylinder

The two-dimensional flow over a circular cylinder is solved as an example of an external flow over a bluff body. The resulting flow field strongly depends on the Reynolds number. For $40 \geqslant Re \geqslant 6$ a steady state exists, with a pair of symmetric separation bubbles on the leeward side. At higher Reynolds numbers the flow field is inherently unsteady and is characterized by cyclic vortex shedding.

In the present work, the time-dependent flow field over a two-dimensional circular cylinder is computed for a range of Reynolds numbers $1000 \geqslant Re \geqslant 40$ (based on the diameter). The symmetrical flow is solved for an impulsively started cylinder at $Re = 40$ and $Re = 550$ while the asymmetric case with vortex shedding is simulated for $Re = 100$, 200, 550, and 1000. The no-slip condition is given on the cylinder and uniform velocity is specified on the far-field boundary.
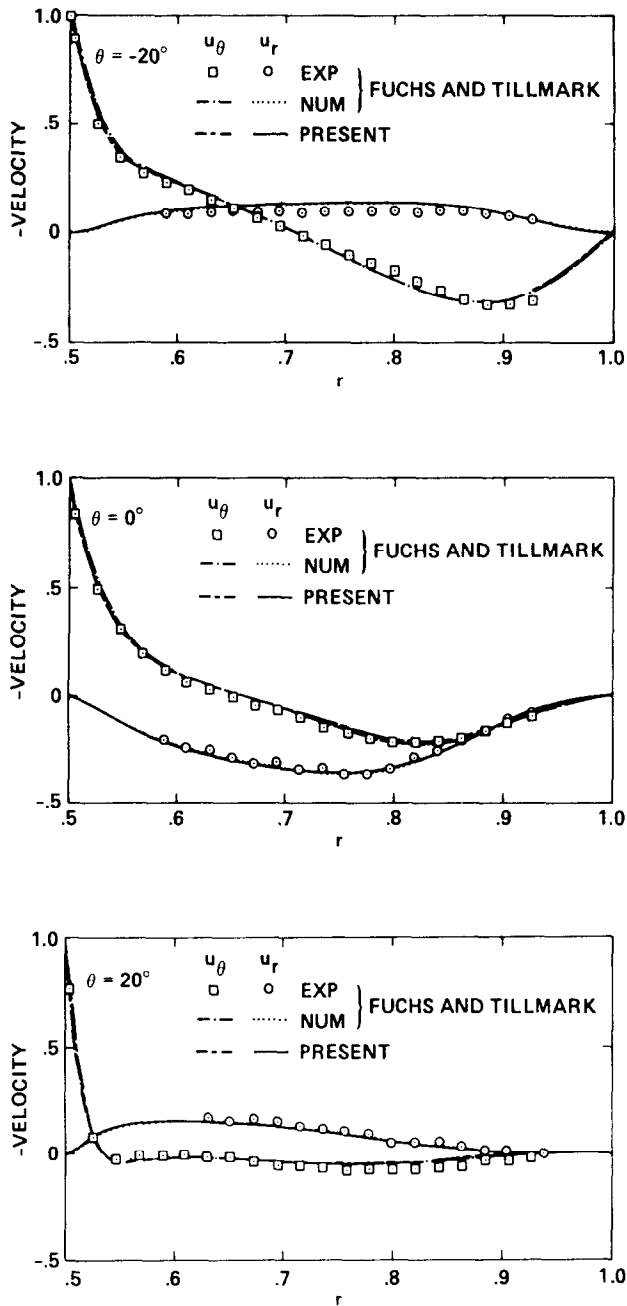
FIG. 7. Comparison of the velocity distribution along the radial lines $\theta = -20^\circ$, 0°, and 20°.

Symmetric Flow

The symmetric flow for Re = 40 is solved using a nonorthogonal coordinate system with $45 \times 73 \times 3$ mesh points in the radial, circumferential, and axial directions, respectively. A non-concentric circular outer boundary with a radius of 20 units (cylinder diameters) is constructed. The center of the outer boundary is shifted into the wake region 15 units from the center of the cylinder. The case with Re = 550 uses a cylindrical grid with a concentric outer boundary at a distance of 50 diameters and $81 \times 85 \times 3$ mesh points. In both cases, mesh points are clustered near the cylinder and in the wake region.

The time evolution of the separation length (measured from the rear of the cylinder and normalized by the diameter) for Re = 40 is compared with the numerical results of Collins and Dennis [25] and with the experimental results of Coutanceau and Bouard [26] in Fig. 8. Good agreement is obtained, especially at the initial stages of the flow evolution ($t < 8$). The slight discrepancy for $t > 8$ is attributed to "wall effects" which exist in the experimental case because of the water tunnel walls and in the present numerical solution because of the Dirichlet-type boundary conditions at the outer boundary.

At a higher Reynolds number, stable symmetrical flow exists only for a short period of time. In Fig. 9 the time evolution of the separation length for Re = 550 is compared with the numerical solution obtained by Loc [27] using a two-dimensional stream-function vorticity formulation and with the experimental results of Bouard and Coutanceau [28]. The two numerical solutions compare favorably, but slightly under estimate the experimental results. A good agreement in the numerical results is observed although totally different methods and grids are used. In the present study a substantially coarser mesh is employed and a spatially second-order-accurate scheme is used, while Loc [27] uses a fourth-order-accurate scheme.
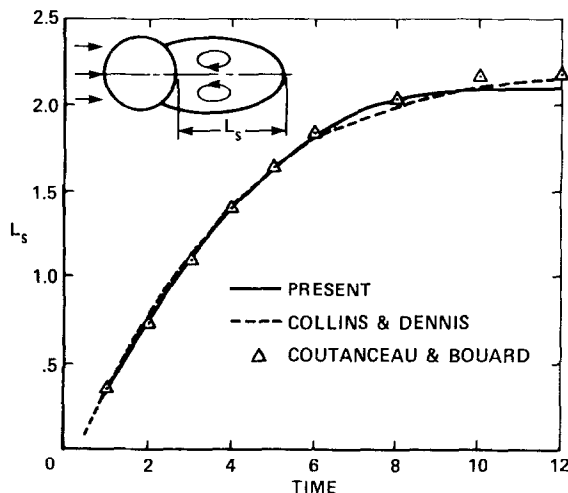

FIG. 8.   Time evolution of the separation length behind the circular cylinder at Re = 40.

Asymmetric Flow

At a Reynolds number higher than 40 any perturbation excites an unsteady flow and eventually a periodic vortex shedding is established generating the well-known von Kármán vortex street. This phenomenon has been addressed in several previous numerical and experimental works; see Refs. [5, 19, 20, 26] for a more comprehensive review.

In the present study, the laminar vortex shedding over a circular cylinder is simulated at Reynolds numbers of 100, 200, 550, and 1000. The analysis of the flow field properties and the explanation of the dynamical phenomena associated with it are beyond the scope of the present paper. The main concern here is in validating the numerical method and studying its properties and capabilities.

A cylindrical coordinate system is used with $81 \times 85 \times 3$ mesh points in the radial, circumferential and axial directions, respectively. The concentric outer boundary is at a distance of 50 diameters from the center of the cylinder. Mesh points are clustered near the body and in the wake region. The minimal radial spacing near the cylinder is 0.014, while the maximal radial spacing at the outer boundary is 2.15. The ratio between the maximal and the minimal Jacobian is of the order $10^4 - 10^5$, which is quite high and might create numerical difficulties resulting in inaccurate solutions, unless the geometric quantities are approximated consistently.

The vortex shedding is triggered by an asymmetric perturbation which consists of rotating the cylinder a short period of time in the clockwise and then in the counterclockwise directions, [5]. The computation is performed within a limited nondimensional time $(t < 40)$ in order to minimize the wall effects. It was found that a small amount of fourth-order artificial diffusion should be added for

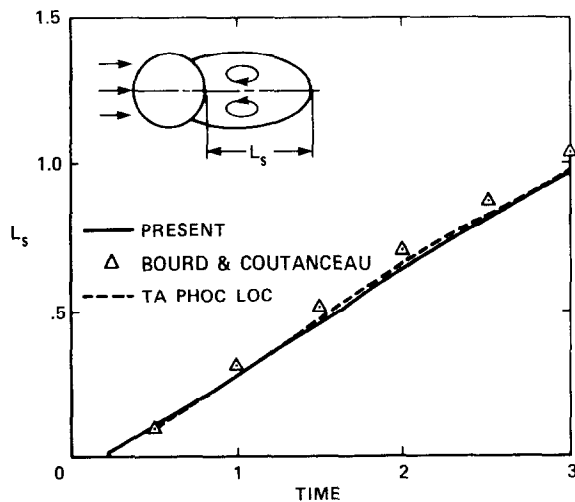

FIG. 9.   Time evolution of the separation length behind the circular cylinder at $Re = 550$.

Re > 200 in order to smooth out the solution in the far wake region, where the grid is coarse.

The time evolution of the lift and the drag coefficients as a function of the Reynolds number is given in Fig. 10. In each case, following a relatively short transient flow, the onset of periodic flow dominated by a single frequency can be observed. The amplitude of the oscillations and the Strouhal number of the vortex shedding increase with the Reynolds number. Figure 11 compares the Strouhal number obtained in the present study with other numerical and experimental results [10, 20, 29]. Considering the complexity of the problem and the wide spread in the results, reasonable agreement is obtained, although the present results predict a slightly high Strouhal number for Re > 500.

Figure 12 shows a partial view of the grid in the vicinity of the circular cylinder for the case of Re = 200. Figures 13a and b compare the instantaneous streamlines for five equally spaced instances along one vortex-shedding cycle with the results obtained by Rogers [30] for an identical case. The time is normalized by the period and $t = 0$ corresponds to the instant when the lift coefficient is maximal. The lift coefficient is minimal and the drag coefficient is maximal at $t = \frac{1}{2}$, while at
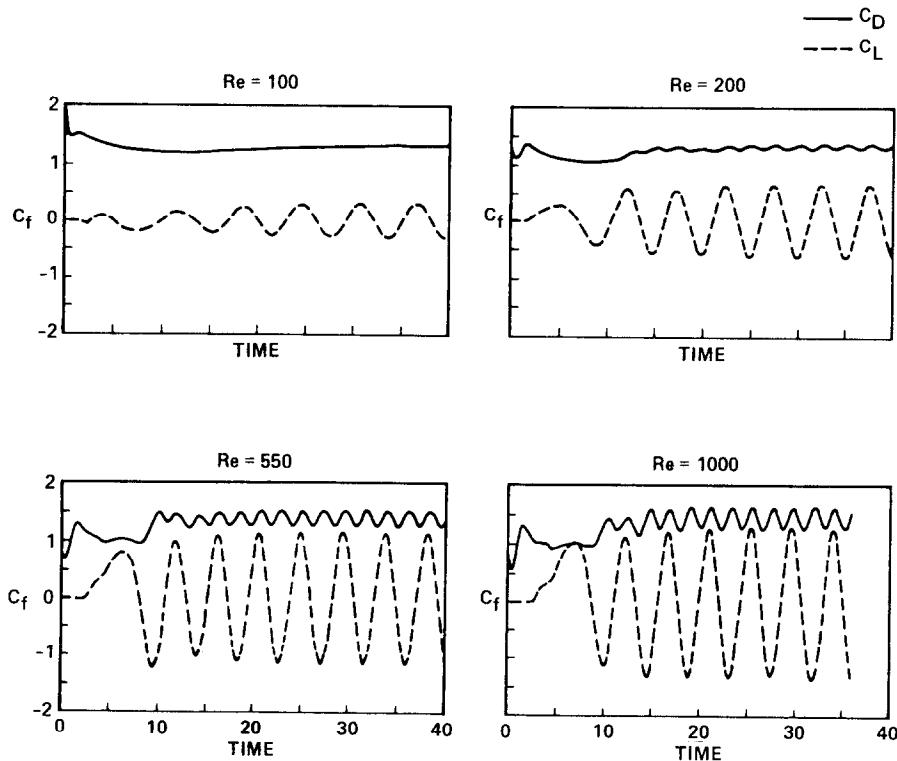

FIG. 10.   Time evolution of the force-coefficients on the circular cylinder at various Reynolds numbers.
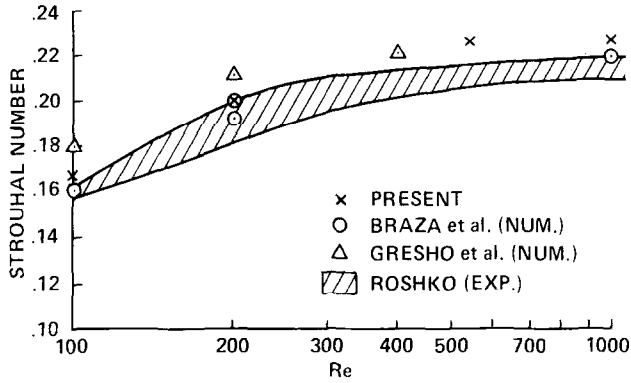
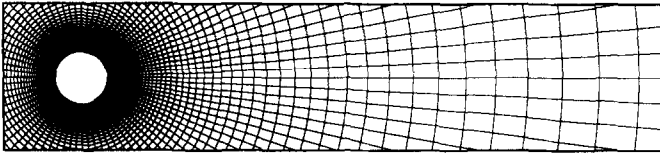FIG. 11.   The dependence of the vortex-shedding Strouhal number on the Reynolds number for a circular cylinder.

FIG. 12.   A partial view of the computational grid over the circular cylinder at Re = 200.
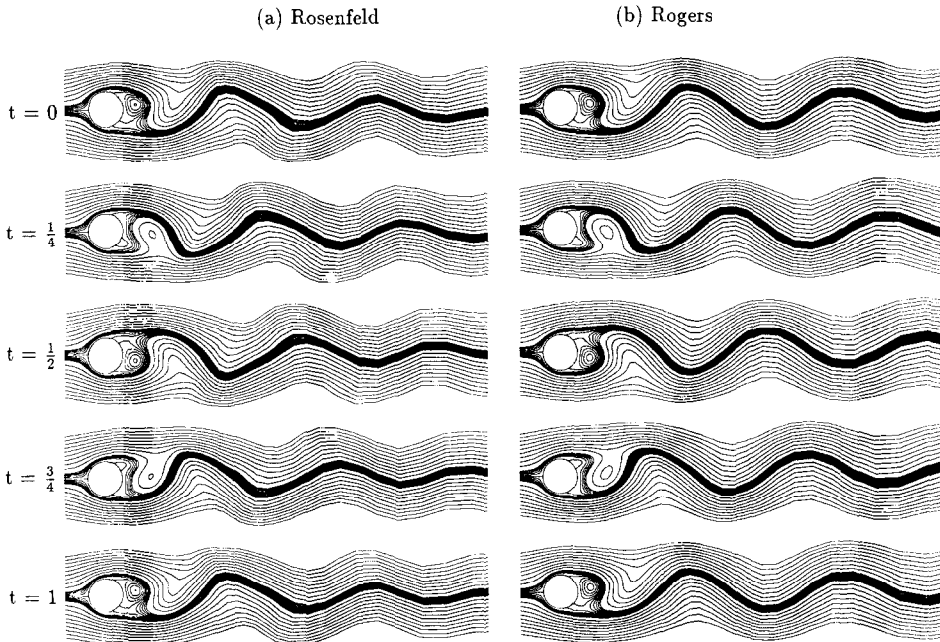
(a) Rosenfeld   (b) Rogers

FIG. 13.   Instantaneous streamlines for one vortex-shedding cycle (Re = 200).

$t = \frac{1}{4}$ and $t = \frac{3}{4}$ the lift coefficient vanishes and the drag coefficient is minimal. The corresponding pressure fields for both solutions are shown in Fig. 14 for the same instances. The centers of the concentric pressure contours in the wake region correspond to a local minimum in the pressure.

The periodic characteristics of the flow can be clearly seen. The flow fields at the beginning of the cycle ($t = 0$) and at the end of the cycle ($t = 1$) are essentially identical. Moreover, the flow field at $t = \frac{1}{2}$ is a mirror image of the flow field at $t = 0$. A similar relationship is found between the flow fields at $t = \frac{1}{4}$ and $t = \frac{3}{4}$, when the instantaneous lift coefficient vanishes. A large separation bubble is created at the upper side of the cylinder at $t = 0$. The bubble induces a low pressure field, which causes a large positive lift coefficient, as well as maximal drag. The bubble ultimately separates from the body and is washed downstream ($t = \frac{1}{4}$). The lift coefficient is decreased to zero and the drag coefficient is minimal at that time, (Fig. 10). At $t = \frac{1}{2}$ a large separation bubble is created at the lower side, reversing the direction of the lift coefficient. This bubble is washed downstream as well and creates the lower vortex of the von Kármán vortex street. The centers of the shed vortices are characterized by a low pressure region.

Rogers [30] solved an identical case using the same grid and time-step but a different numerical method. His method is based on the artificial compressibility procedure with a fifth-order upwind scheme, second-order temporal accuracy, and
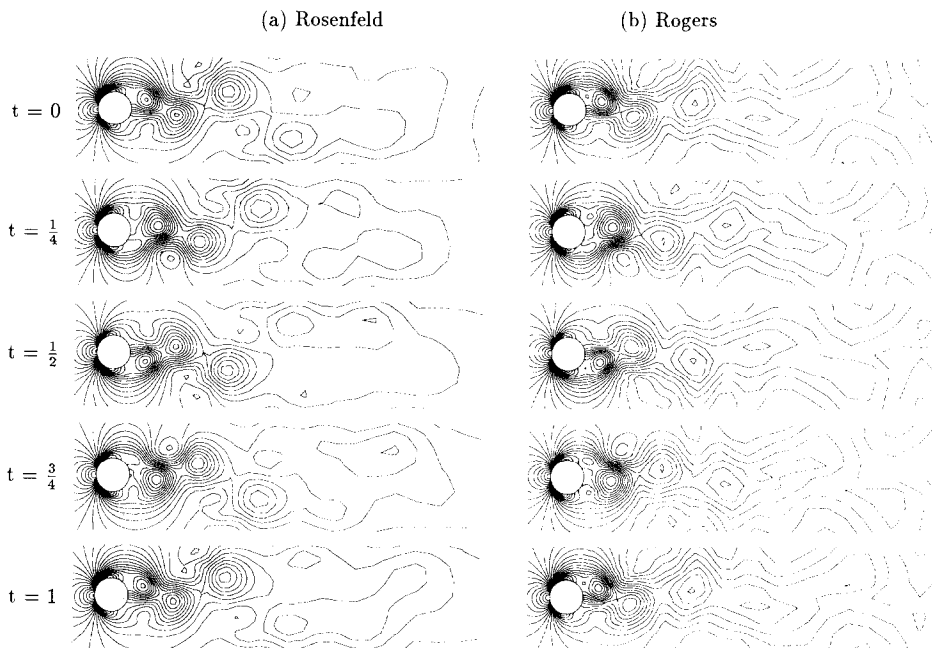
(a) Rosenfeld   (b) Rogers

FIG. 14. Pressure contours for one vortex-shedding cycle (Re = 200).

TABLE I

Comparison of the Lift (C_L) and Drag (C_D) Coefficients and the
Strouhal Number (St) for the flow over a circular cylinder at
Re = 200

	C_D	C_L	St
Gerrard [31] (exp.)			0.18–0.20
While [32] (exp.)	1.3		
Lecointe and Piquet [5]			
2nd order	1.46 ± 0.04	±0.70	0.23
4th order	1.58 ± 0.0035	±0.50	0.19
Gresho et al. [10]	1.76 ± 0.09	±1.05	0.21
Braza et al. [20]		±0.77	0.20
Rogers [30]	1.33 ± 0.05	±0.68	0.19
Present	1.31 ± 0.04	±0.65	0.20
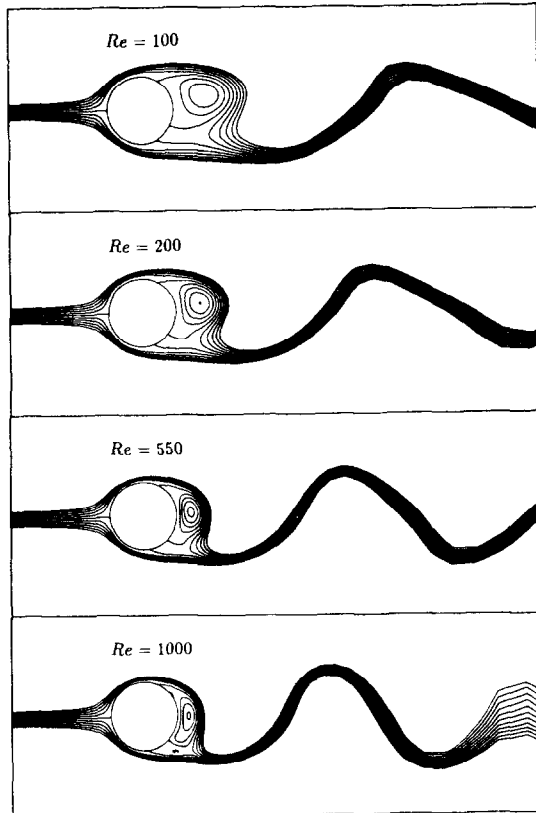
FIG. 15. The effect of Reynolds number on the streamlines at maximal lift coefficient.

characteristic boundary conditions [6, 7]. Despite the differences in the numerical algorithms good agreement is obtained, as shown in Figs. 13–14. The results compare particularly well in the regions near the circular cylinder, where the resolution of the grid is adequate in both solutions. The apparent discrepancy in the stream function contours at the center of the vortices is due to a small difference in the time of the corresponding plots (although the time increment is equal, the starting times of the shedding cycles are not the same since the triggering mechanism of the vortex shedding is different). The agreement deteriorates somewhat at the far wake region, where the mesh size is of the order of the cylinder's diameter and truncation errors affect the solution differently for each case.

Some dissipation of the downstream vortices can be observed in both solutions. The amplitude of the wake decreases and the steep pressure gradient in the vortices flattens out with increasing distance from the cylinder. This dissipation is mainly a result of the coarse grid at the far wake region (Fig. 12).

Table I compares the Strouhal number and the drag and lift coefficients for the $Re = 200$ case with several other experimental and computational results
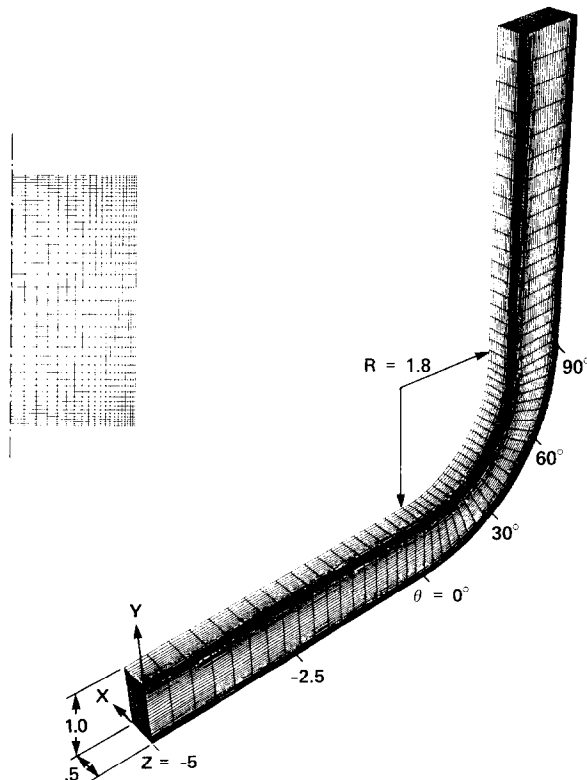

FIG. 16. The geometry and the grid for the square duct with 90° bend.

[5, 10, 20, 30–32]. Gerrard's results [31] summarize experimental results obtained from several sources. The scatter in both the numerical and the experimental results is quite large, demonstrating the complexity of the problem. The present computations are within the range of other available data. Note in particular the good agreement with the recent solution of Rogers [30].

Figure 15 shows the effect of the Reynolds number on the instantaneous streamline contours for a time which corresponds to the maximal lift coefficient at
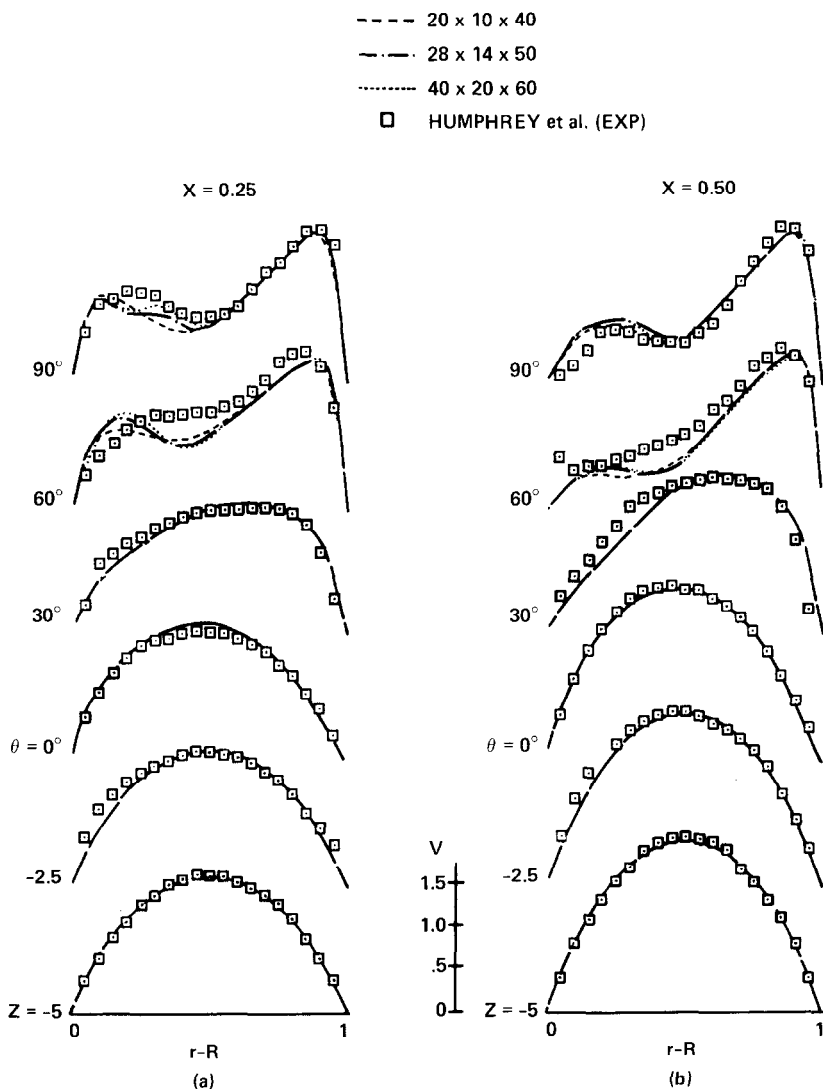

FIG. 17.   Convergence of the streamwise velocity profiles with mesh refinement.

each Reynolds number. The laminar solution is computed in each case, although in the real flow the far wake does not remain laminar for Reynolds number higher than a few hundreds. The extent of the diffusion effects decrease with the increase of the Reynolds number. The attached separation bubble, where the diffusion effects are prominent, is the largest for $Re = 100$ and gradually decreases as the Reynolds number increases. The center of the attached separation bubble moves toward the lower side of the cylinder as the Reynolds number increases along with a downward bending of the streamlines. The wavelength of the wake decreases with increasing Reynolds number, in accordance with the increase in the Strouhal number (see Fig. 11).
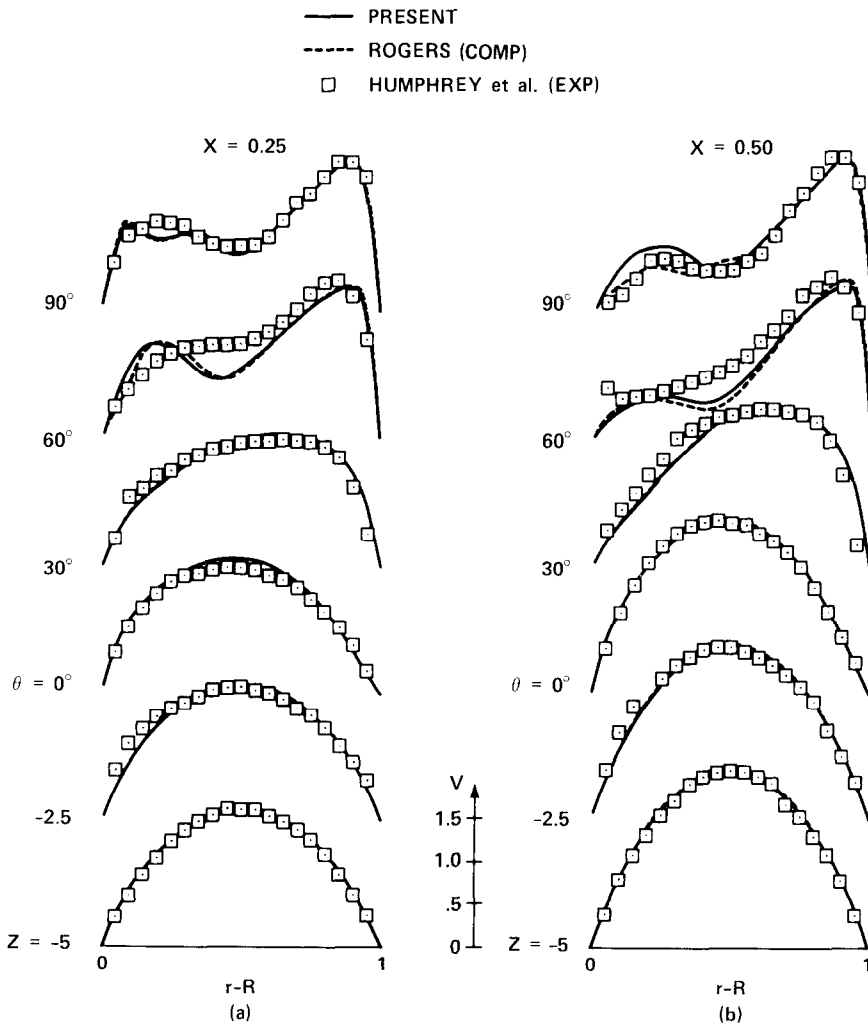

FIG. 18. Comparison of the streamwise velocity distribution along (a) $x = 0.25$ and (b) $x = 0.50$.

Flow in a Square Duct with 90° Bend

A square cross section duct with a 90° bend is solved as a test case for a three-dimensional internal flow. Flows in curved ducts occur in a wide range of practical applications such as aircraft intakes, turbomachinery blade passages, diffusers, and heat exchangers. A distinguishing characteristic of the flow in ducts with strong curvature is the generation of streamwise vorticity caused by the centrifugal forces which generate substantial secondary flow and redistribution of the longitudinal velocity.

The geometry and the grid used in the present study are shown in Fig. 16. The symmetry of the problem across the $x = 0.5$ plane is utilized to save mesh points. The length of the side of the square cross section is set to one unit. The straight inflow and outflow sections before and after the bend are five units long, and the radius of curvature of the inner wall in the 90° bend is 1.8 units. Three different grids with mesh sizes of $21 \times 11 \times 41$, $29 \times 15 \times 51$, and $41 \times 21 \times 61$ were used for solving the problem. The finest mesh is shown in Fig. 16 along with an enlarged view of the grid at the crossflow plane.

The Reynolds number is 790, based on the average velocity at the inlet. The fully developed laminar flow in a straight square duct is specified at the upstream boundary, while zero gradient of the velocity is given at the downstream boundary. The probem is solved time accurately, but only the steady state solution is presented here, for comparison with the experimental data of Humphrey et al. [32]. The
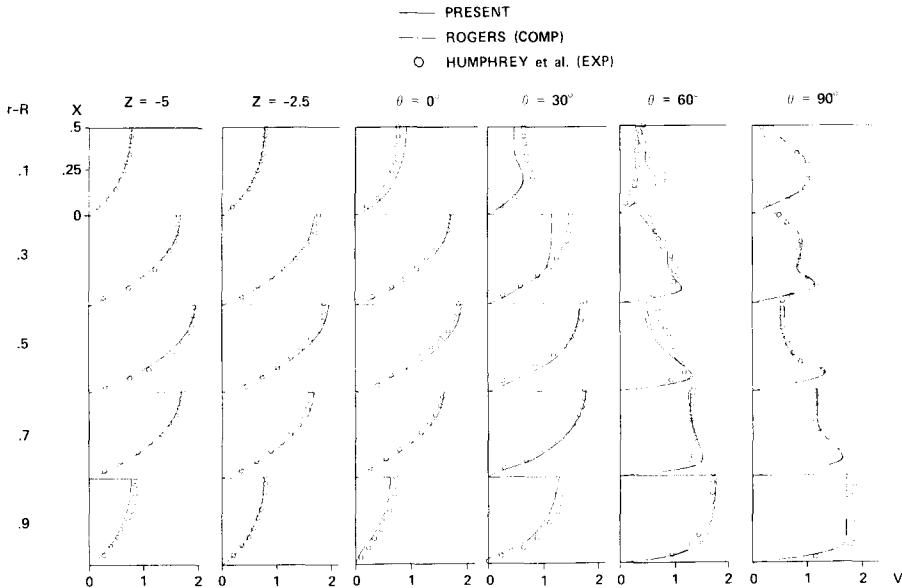

FIG. 19. Comparison of the streamwise velocity distribution along x lines at several radial and streamwise cross sections.

experimental data are limited to the distribution of the streamwise velocity over several sections of the duct.

The computed streamwise velocity profiles over three different meshes are shown in Fig. 17. The streamwise velocity profile is presented in this figure for six cross sections along the duct. The location of these cross flow planes is shown in Fig. 16. At each plane, the streamwise velocity is given along two lines, $x = 0.25$ (Fig. 17a) and $x = 0.50$ (Fig. 17b). In most of the flow regions shown, the results of the two finer meshes are in very good agreement with the experimental results of Humphrey et al. [32], indicating that the solution is essentially grid-independent.

Figure 18 compares the streamwise velocity obtained from the finest grid computation with the numerical results of Rogers [30] (who used the same grid) and the experimental results of Humphrey et al. [32] at the same six cross flow planes along the duct. The agreement between the two numerical results is very good in most of the regions. The agreement with the experimental results is good, especially at the first four cross sections. Some discrepancy is found between the numerical and the experimental results at the two downstream planes. Nevertheless, the large peak of the streamwise velocity near the outer boundary is well predicted in the numerical computations.

Figure 19 compares the present streamwise velocity solution with the numerical computation of Rogers [30] and the experimental results of Humphrey et al. [32] for the same cross sections. For each cross section, the distribution of the velocity along the x axis is given for five different radial locations. The agreement in the numerical results is remarkable, bearing in mind that totally different solution
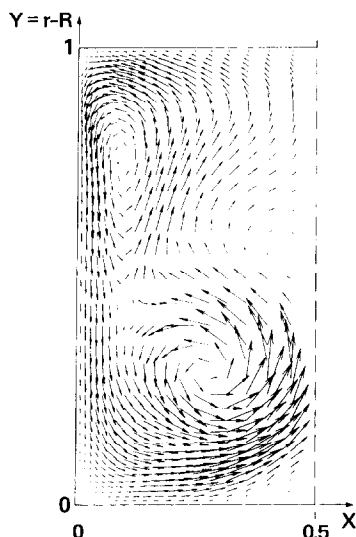

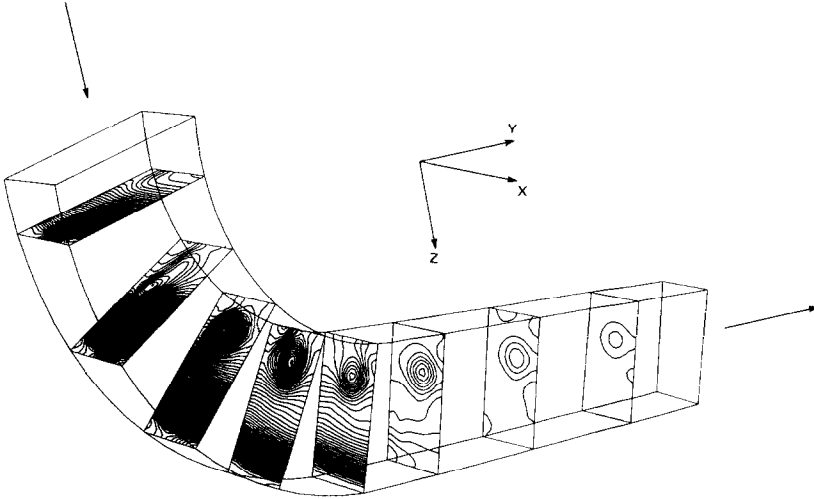FIG. 20. The crossflow velocity at the plane $\theta = 90°$.

FIG. 21.   Pressure contours at several cross sections.

methods have been used. The agreement with the experimental results is also good in most of the flow regions.

Figure 20 plots the crossflow velocity at the plane $\theta = 90°$. At that plane, a very complicated pattern of the secondary flow is already established. Three different vortices can be seen. A large and relatively strong vortex is found near the inner wall. A second vortex is found near the side wall, while a relatively weak vortex exists near the symmetry plane, at about the center of the duct. Figure 21 gives the pressure contours at several corssflow planes in the bend region and in the region downstream of the bend. The main vortex is generated in the bend and subsequently diffuses in the downstream section.

6. SUMMARY

A method for solving the three-dimensional, unsteady, incompressible Navier–Stokes equations is presented for generalized curvilinear coordinate systems. Accuracy is achieved by finite-volume discretization on a staggered mesh along with consistent approximation of the geometric quantities. The formulation with the volume fluxes as dependent variables results in a simple extension of the staggered-mesh approach to generalized coordinate systems and facilitates satisfying the mass conservation equation to machine accuracy for all the computational cells. The fractional step method is combined with an approximate factorization of the momentum equations. Each step of the method is consistent and therefore the physical boundary conditions can be used. An efficient Poisson solver has been developed for generalized nonorthogonal coordinate systems using a consistent

discrete approximation. The discrete approximation of the governing equations is second-order accurate in both time and space. However, in the present study the pressure computation is replaced by an approximate equation, reducing the temporal accuracy of the pressure to first order.

Several two- and three-dimensional laminar validation cases have been presented for both steady and unsteady flows. Good agreement with other numerical and experimental results is obtained over a wide range of Reynolds numbers. Future work will include solution of time-dependent, three-dimensional flow fields for more complicated geometries.

Appendix A

In the present implementation of the fractional step solution method, the computed velocity field is the exact solution of the discretized governing equations, provided the pressure field at the two previous time levels is the correct one and the system (26a) is solved exactly (without splitting errors). However, the computed pressure field is not the exact solution of the original equations, but only a first-order-accurate approximation in time.

For ease of presentation, the equations are discretized only in time and written in a vector form equivalent to Eqs. (18a) and (11),

$$\frac{\mathbf{u}^{n+1}}{\varDelta t} = G + \theta_d \nabla^2 \mathbf{u}^{n+1} + \theta_r \nabla(\varDelta P), \tag{A1}$$

$$\nabla \cdot \mathbf{u}^{n+1} = 0, \tag{A2}$$

where G holds all the terms from the previous time levels $n, n-1$, and $\varDelta P = P^{n+1} - P^n$. Without losing generality, it is also assumed that $\alpha_u = \alpha_p = 0$. The velocity vector can always be split into

$$\mathbf{u}^{n+1} = \mathbf{u}_\omega + \mathbf{u}_\phi \tag{A3}$$

such that $\mathbf{u}_\phi$ is irrotational (see (A5)). Equations (A1) and (A2) can be split and solved *exactly* (since (A1) is linear) by the following fractional steps

$$\frac{\mathbf{u}_\omega}{\varDelta t} = G + \theta_d \nabla^2 \mathbf{u}_\omega \tag{A4}$$

$$\frac{\mathbf{u}_\phi}{\varDelta t} = \theta_r \nabla \phi \tag{A5}$$

$$\nabla \cdot \mathbf{u}_\phi = -\nabla \cdot \mathbf{u}_\omega, \tag{A6}$$

$$0 = \theta_d \nabla^2 \mathbf{u}_\phi + \theta_r \nabla(\varDelta P - \phi), \tag{A7}$$

with the proper boundary conditions. This splitting of the equations introduces a

new unknown ϕ. Note that (A4) is an uncoupled equation, and (A5) and (A6) should be solved as a coupled system for the unknowns $\mathbf{u}_\phi$ and ϕ. Equation (A7) is a stand-alone equation for the unknown ΔP.

In the present application of the fractional step method, only the steps (A4)–(A6) are actually solved. Instead of solving (A7) for the pressure, the first-order time-accurate substitution $\Delta P = \phi$ has been used. However, it is easy to verify that steps (A4)–(A6) yield an exact solution of the velocity, provided P^n and P^{n-1} are known and the proper boundary conditions are specified for $\mathbf{u}_\omega$. The boundary conditions for $\mathbf{u}_\omega$ in (A4) are approximated to be the conditions given for the unsplit velocity. Consequently, an error of order Δt is introduced at the boundaries.

In the practical application of the method, there is an additional error in the velocity field because P^n is not the exact solution (for $n > 1$). However, the error in the velocity (excluding near the boundaries) is still second-order accurate in time (see (A5) and (A7)).

ACKNOWLEDGMENTS

REFERENCES

1. D. KWAK, J. L. CHANG, S. P. SHANKS, AND S. CHAKRAVARTHY, *AIAA J.* **24**, No. 3, 390 (1986).
2. M. ROSENFELD, M. ISRAELI, AND M. WOLFSHTEIN, *J. Comput. Phys.* **88**, 255 (1990).
3. W. SHYY, S. S. TONG, AND S. M. CORREA, *Numer. Heat Transfer* **8**, 99 (1985).
4. M. HASHIGUCHI, T. OHTA, AND K. KUWAHARA, "Computational Study of Aerodynamic Behavior of a Car Configuration," AIAA Paper 87-1386, 1987 (unpublished).
5. Y. LECOINTE AND J. PIQUET, *Comput. Fluids* **12**, 255 (1984).
6. S. E. ROGERS AND D. KWAK, "An Upwind Differencing Scheme for the Time Accurate Incompressible Navier–Stokes Equations," AIAA Paper 88-2583, 1988 (unpublished).
7. S. E. ROGERS AND D. KWAK, "Numerical Solution of the Incompressible Navier–Stokes Equations for Steady-State and Time-Dependent Problems," AIAA Paper 89-0463, 1989 (unpublished).
8. C. L. MERKLE AND M. ATHAVALE, "Time-Accurate Unsteady Incompressible Flow Algorithms Based on Artificial Compressibility," AIAA Paper 97-1137, 1987 (unpublished).
9. A. J. CHORIN, *Math. Comput.* **22**, 745 (1968).
10. M. P. GRESHO AND R. L. SANI, *Int. J. Numer. Methods Fluids* **7**, 1111 (1987).
11. J. KIM AND P. MOIN, *J. Comput. Phys.* **59**, 308 (1985).
12. S. A. ORSZAG, M. ISRAELI, AND M. O. DEVILLE, *J. Sci. Comput.* **1**, 75 (1986).
13. S. V. PATANKAR AND D. B. SPALDING, *Int. J. Heat Mass Transfer* **15**, 1787 (1972).
14. F. H. HARLOW AND J. E. WELSH, *Phys. Fluids* **8**, 2182 (1965).
15. M. VINOKUR, *J. Comput. Phys.* **81**, 1 (1989).
16. M. ROSENFELD AND D. KWAK, "Numerical Solution of Unsteady Incompressible Viscous Flows in Generalized Moving Coordinate Systems," AIAA Paper 89-0466, 1989 (unpublished).
17. R. M. BEAM AND R. F. WARMING, *SIAM J. Sci. Statist. Comput.* **1**, 131 (1980).
18. M. ROSENFELD, D. KWAK, AND M. VINOKUR, "Development of an Accurate Solution Method for the

Unsteady Three-Dimensional and Incompressible Navier–Stokes Equations in Generalized Coordinate Systems," NASA TM, 1989 (unpublished).

19. R. PEYRET AND T. D. TAYLOR, *Computational Methods for Fluid Flow* (Springer-Verlag, New York, 1983), p. 786.
20. M. BRAZA, P. CHASSAING, AND H. HA MINH, *J. Fluid Mech.* **165**, 79 (1986).
21. M. ROSENFELD AND D. KWAK, in Proc. of the Eleventh International Conferece on Numerical Methods in Fluid Dynamics, Williamsburg, Virginia, USA, 1988, (Springer-Verlag, 1989).
22. J. B. CAZALBOU, M. BRAZA, AND H. H. MIHN, in *Proceedings, 3th Int. Conf. on Numerical Methods in Laminar and Turbulent Flow, Seattle, Washington, 1983,* edited by C. Taylor *et al.* (Pineridge Press, UK, 1983), p. 786.
23. D. P. HWANG AND H. T. HUYNH, in *Proceedings, 5th Int. Conf. on Numerical Methods in Laminar and Turbulent Flow, Montreal, Canada, 1987,* edited by C. Taylor *et al.* (Pineridge Press, UK, 1987), p. 244.
24. L. FUCHS AND N. TILLMARK, *Int. J. Numer. Methods Fluids* **5**, 311 (1985).
25. W. M. COLLINS AND S. C. R. DENNIS, *J. Fluid Mech.* **60**, 105 (1973).
26. M. COUTANCEAU AND R. BOUARD, *J. Fluid Mech.* **79**, 257 (1977).
27. T. P. LOC, *J. Fluid Mech.* **100**, 111 (1980).
28. R. BOUARD AND M. COUTANCEAU, *J. Fluid Mech.* **101**, 583 (1980).
29. A. ROSHKO, "On the Development of Turbulent Wakes from Vortex Streets," NACA TN 2913, 1953 (unpublished).
30. S. E. ROGERS, NASA Ames Research Center, Moffett Field, CA, priate communication (1989).
31. J. H. GERRARD, *Philos. Trans. Roy. Soc.* **288**, 351 (1978).
32. R. WILLE, *Adv. Appl. Mech.* **6**, 273 (1960).
33. J. A. C. HUMPHREY, A. M. K. TAYLOR, AND J. H. WHITELAW, *J. Fluid Mech.* **83**, 509 (1977).